

# **Ocean water clarity and the ocean general circulation in a coupled climate model**

Anand Gnanadesikan and Whit G. Anderson

NOAA/Geophysical Fluid Dynamics Lab and Princeton University, Princeton, NJ

Forrestal Campus, Princeton University

201 Forrestal Road, Princeton, NJ 08540

Anand.Gnanadesikan@noaa.gov

Revised for J. Phys. Oceanography

July 15, 2008

## **Abstract**

Ocean water clarity affects the distribution of shortwave heating in the water column. In a one-dimensional time-mean sense, increased clarity would be expected to cool the surface and heat subsurface depths as shortwave radiation penetrates deeper into the water column. However, wind-driven upwelling, boundary currents and the seasonal cycle of mixing can bring water heated at depth back to the surface. This warms the equator and cools the subtropics throughout the year while reducing the amplitude of the seasonal cycle of temperature in polar regions. This paper examines how these changes propagate through the climate system in a coupled model with an isopycnal ocean component. We focus on the different impacts associated with removing shading from different regions. Increasing shortwave penetration along the equator causes warming to the south of the equator. Increasing it in the relatively clear gyres off-equator causes the Hadley cells to strengthen and the subtropical gyres to shift equatorwards. Increasing shortwave penetration in the less clear regions overlying the oxygen minimum zones causes the cold tongue to warm and the Walker circulation to weaken. Increasing shortwave penetration in the high latitude Southern Ocean causes an increase in the formation of mode water from subtropical water. The results suggest that more attention be paid to the processes distributing heat below the mixed layer.

## Introduction

If ocean water were perfectly clear, solar radiation in the blue and near-UV bands would penetrate to great depths with e-folding scales exceeding 50m (Morel, 1988, Morel et al., 2007). In general, however, the depth of penetration is much shallower than this (Jerlov, 1976) due to the presence of phytoplankton pigments, colored dissolved organic matter, and scatterers such as plankton, bacteria, viruses and suspended particles. This paper considers how the additional shortwave absorption represented by these substances affects the large-scale circulation of the ocean, and how this answer depends on where it is located.

One would expect that decreasing water clarity would result in more trapping of radiation near the surface, increasing surface temperatures, and cooling the deep. A number of authors (Lewis et al., 1990; Stramska and Dickey, 1993; Siegel et al., 1995; Strutton and Chavez, 2004) have presented one-dimensional analyses demonstrating that changing penetration depths could have a significant impact on the temporal evolution of the mixed layer. More complex models, however, show a more complicated picture. A series of studies with ocean-only models (Nakamoto et al. 2001; Sweeney et al., 2005; Manizza et al. 2005) found that increasing water clarity *increased* the surface temperatures in the cold tongue by up to 1.2°C, with very small changes in sea surface temperature away from this region. This is the opposite of the response that would be expected from a one-dimensional balance. Sweeney et al. (2005) argued that the reason for this change was a decrease in the advective cooling associated with the cold tongue, resulting both from a warming of deeper upwelling water and a reduction of the rate at

which cold water is upwelled. The changes in surface temperature occur almost immediately, as do those in upwelling flux. Because of this, Sweeney et al. (2005) argued that it was relatively fast changes in mixed layer depth, which in turn determines what fraction of the Ekman upwelling is supplied by warm surface waters as opposed to cooler thermocline waters, that governs the temperature response.

There are reasons to believe that ocean water clarity has changed in the past. Paleoproductivity estimates (Paytan and Griffith, 2007) suggest that significant (up to a factor of 5) changes in particle export occur in a number of cores, implying large changes in chlorophyll concentration at these locations. Karl et al. (2001) suggest that chlorophyll concentrations at station ALOHA could have doubled between the 1950s and the present. On even shorter time scales, analysis of interannual variability in the SeaWiFS chlorophyll-a retrievals from 1998-2004 (McClain et al., 2004) shows that even over this relatively small period, over 40% of the ocean the observed range of chlorophyll is more than 40% of the mean value. A particularly striking feature is the high variability occurring along the boundary between the high and low chlorophyll zones. Polovina et al. (2008) note that there are trends in the SeaWiFS dataset, suggesting that the very clear regions are expanding.

Whether changes in SST produced by changing ocean color can have a major impact on the climate system will be determined by whether or not they are amplified or damped by the atmosphere. Shell et al. (2003) suggested that the initial response of the atmosphere should be to increase the SST perturbations, as they would be expected to trigger Bjerknes-type feedbacks. However, a result showing that the initial response to a climate perturbation will amplify does not necessarily imply that the long-term response

will be large. As the El Niño Southern Oscillation system shows, both positive and negative feedbacks act on changes in equatorial circulation. As a result, a long-term mean El Niño-like perturbation will be damped if the reduction in upwelling results in a decrease in the volume of light water and a shallowing of the thermocline (Federov et al., 2006).

Two lines of research have examined this question with coupled climate models. One line, represented by Murtugudde et al. (2002) and Ballabrera-Poy et al. (2007) uses a hybrid coupled model examine the impacts of changing the penetration from a uniform penetration depth of 17m to one based on chlorophyll estimated using the CZCS satellite. Timmermann and Jin (2002) and Marzeion et al. (2005) extended these results to look at the impact of interactive chlorophyll. These papers allow for changes in the mean state of the ocean but ignore atmospheric thermodynamic feedbacks and, in general, find relatively small changes in such features as sea surface currents and overturning, though not necessarily small changes in tropical variability. Because of the spatial structure of the observed chlorophyll field, the perturbation that is used in these simulations often results in a decrease in water clarity and shortwave penetration at the equator and an increase off-equator in the subtropical gyres relative to the fixed-attenuation scale controls.

A second line of research has examined the impact of changing shortwave absorption in a fully coupled climate model. Wetzel et al. (2006) examine this effect in the Max Planck Institute model, changing the e-folding scale from 11m to a spatially-varying field. They find an average increase in surface temperatures in the cold tongue of 0.5°C with maximum changes between 0.6°C and 1°C. Lengaigne et al. (2007) also use a

full coupled climate model and examine the difference between using a constant attenuation depth and predicted chlorophyll concentrations. They find a warming of the cold tongue of about 1°C and very weak-off equatorial cooling. As with the hybrid models their simulated chlorophyll fields also result in a decrease in penetration along the equator and an increase in penetration in the gyres relative to the constant-attenuation control (and interestingly also relative to observations). The results of Sweeney et al. (2005) suggest that this could produce some compensation between increasing upwelling due to increased attenuation near the equator (which would cool the cold tongue) and increasing subsurface temperatures through deeper penetration of shortwave radiation off equator (which would warm the cold tongue). None of these coupled simulations has looked at the *total* impact of absorbers and scatterers, as the “clear” water controls used still absorb a great deal. It is thus possible that all of these coupled simulations have underestimated the importance of ocean water clarity on the large-scale circulation due to their experimental design.

In recent work (Anderson et al., 2007) we examined the impact of removing *all* of the additional absorption associated with dissolved and suspended substances in a coupled climate model- thus increasing the penetration depth of shortwave radiation everywhere. We found that this warmed the cold tongue by up to 1.8°C and cooled some extratropical regions by about a comparable amount (approximately 2-3 times the signal seen by Wetzel et al., 2006 and Lengaigne et al., 2007). Following Sweeney et al. (2005), we also highlighted the importance of shortwave absorption in the clear centers of the subtropical gyres, as compared to absorption right along the equator.

This paper extends these results to examine three main questions. First, we examine how these changes in surface temperature affect the ocean circulation as a whole- both directly and through changing the wind field. Second, we examine the degree to which this response is linear in chlorophyll concentration. Finally, we examine in detail how different regions on and off the equator have different impacts on the climate system. In addition to providing information about possible biological-physical couplings, this work reveals some interesting sensitivities to the distribution of heating within the water column that may have implications for the representation of physical mixing in coupled climate models.

## **2. Model Description**

The atmospheric and land components of the model are identical to those used for the CM2.1 global coupled climate model developed for the Fourth Assessment Report of the Intergovernmental Panel on Climate Change and reported in Delworth et al. (2006). The atmosphere is built around a 24-level,  $2^\circ \times 2.5^\circ$  finite volume core with state-of-the-art representations of radiation, convection, and gravity wave drag. The land model is the LM2 model based on the work of Milly and Shmakin (2002), which fixes land properties such as albedo, surface roughness and stomatal resistance (which controls evapotranspiration) based on currently observed land types. The model has one of the better atmospheric simulations in the AR4 dataset (Reichler and Kim, 2008) and when coupled has been found to exhibit a reasonable simulation of El Nino and its feedbacks

for both a level-coordinate ocean model (Van Oldenburgh et al., 2005) and an isopycnal ocean model (Anderson et al., in prep.).

The primary difference between these runs and those done for the Fourth Assessment report is the ocean model. The AR4 models used the level coordinate Modular Ocean Model v. 4 code with shortwave absorption based on the observed distribution of chlorophyll as described in Sweeney et al. (2005). The ocean model used in our simulations is the isopycnal layer model of Hallberg (2005). One key feature of this model is that it has essentially no numerical diapycnal mixing, allowing for clean attribution of changes in heat redistribution at depth (Harrison and Hallberg, 2008). Additionally, isopycnal models are able to more accurately resolve and simulate the physics of overflows (Winton et al., 1998). The model was configured with 48 interior isopycnal layers which strive to follow a set of target densities in addition to a four-layer mixed layer/buffer layer in which densities are free to vary. The code includes a nonlinear equation of state, and Richardson number dependent shear mixing. The impact of unresolved mesoscale eddies is parameterized using a biharmonic Smagorinsky viscosity and along-isopycnal mixing of both tracers and interface height (corresponding to the Gent and McWilliams, 1990 parameterization of eddy Stokes drift in level-coordinate models). A constant coefficient of  $900 \text{ m}^2/\text{s}$  is used for both terms.

A key difference between the model used in these simulations and previous instantiations of the isopycnal model is that we incorporate the two-band shortwave penetration scheme of Manizza et al. (2005), which is a reanalysis of the data of Morel (1988) that permits very low chlorophyll concentrations. As the near-infrared and red-yellow bands of light have short e-folding depths (less than 5m) and our mixed layer in



these runs has a minimum depth of 10m, these bands are simply treated as a surface flux of heat. The blue-green band (with wavelengths less than 550 nm) is allowed to penetrate, following a profile given by

$$(1a) \quad I(z) = I_{bg} e^{-k_{bg} z} = 0.21 I_0 e^{-k_{bg} z}$$

$$(1b) \quad k_{bg} = 0.0232 + 0.074 * chl^{0.674}$$

Where  $I_0$  is the total absorbed shortwave radiation (21% of which is taken to be blue-green) and  $chl$  is the concentration of chlorophyll-a in mg chl/m<sup>3</sup>. Thus if the chlorophyll is set to 0, blue-green light has an e-folding depth of 43m, while at values of 0.2 mg chl/m<sup>3</sup> the e-folding depth is ~20m. In the base state of the model, the chlorophyll concentrations are taken from the non-El Nino SeaWiFS climatology developed by Sweeney et al. (2005) that is currently distributed with the GFDL ocean codes. As seen in Figure 1a, this results in e-folding depths exceeding the 23m associated with Jerlov type I waters over much of the subtropical gyres.

In order to understand differences between our results and previous simulations, it is important to compare the perturbation in heating rates at different depths. An alternative shortwave penetration parameterization is given by Moore et al. (2002) and Wetzel et al. (2006) for which  $I_{bg} = I_0 * 0.5$  and

$$(2) \quad k_{bg} = 0.04 + 0.03 * chl$$

As shown in Figure 1b, this produces much less of a range in penetration depth over most of the ocean. Figure 1c,d compare the annual average heating rate in °C/yr caused by shortwave heating at two depths (given a  $I_0 = 200 \text{ W/m}^2$ ) using a number of published penetration parameterizations. We can get an estimate of the size of the perturbation studied in a given work by looking at the difference between heating rates associated with

two parameterizations. At 100m, the change in heating studied by Wetzel et al. (2006) is similar to the change between the lowest dashed line and the solid line with triangles, or about  $0.4^{\circ}\text{C}/\text{yr}$ . This is slightly smaller than the  $\sim 0.55^{\circ}\text{C}/\text{yr}$  difference between the Manizza et al. (2005) parameterization (solid line) and our representation of clear water (top dashed line), although our model will see much more spatial variability in heating rate than did Wetzel et al. (2006). Note that despite the smaller penetration depth the background heating rate is larger using Moore et al. (2002) because the fraction of penetrating radiation is much higher. Perturbations in shortwave heating in a number of other studies are also represented on this plot. Schneider and Zhu (1998), in a pioneering study on the impact of shortwave heating, introduced a 15m e-folding depth for solar radiation. At 100m, this corresponds to a change in heating of  $0.13^{\circ}\text{C}/\text{yr}$ - significantly smaller than the perturbation we employ. Murtugudde et al. (2002) examine the difference between a 17m e-folding depth and a spatially dependent penetration depth. This perturbation will have the same general shape as the difference between the dashed line at  $0.11^{\circ}\text{C}/\text{yr}$  and our control case, of order  $0\text{-}0.3^{\circ}\text{C}/\text{yr}$  depending on the location. Thus when we remove chlorophyll altogether, we are producing a significantly larger change in solar heating at 100m over a broader latitudinal range than in any of these simulations except for Wetzel et al. (2006).

At 200m, this difference is even more pronounced (Figure 1d). Replacing our chlorophyll-dependent parameterization with clear water produces a much larger impact on subsurface heating ( $0.07^{\circ}\text{C}/\text{yr}$ ) than any of the previous coupled model studies, which at most involve a subsurface warming 10-15% as large. While  $0.07^{\circ}\text{C}/\text{yr}$  may seem

insignificant, it can result in significant temperature perturbations when integrated over the decadal time scales associated with the subtropical gyres.

All the models described herein were initialized from a modern January climatology based on the World Ocean Atlas dataset. The concentrations of radiatively active trace gas concentrations are fixed at 1990 level throughout the simulations, so that the runs correspond to the 1990ctrl runs in the IPCC AR4 model databases. The models all develop a very strong La Nina in the first 20 years, but afterwards are relatively stable as regards their tropical climate.

The base state (using the monthly varying version of the penetration depths in Figure 1a) is referred to as the *Green* run. The *Green* simulation is comparable to other models run as part of the AR4 process. The RMS sea surface temperature error (Figure 2a) from years 200-300 of the control run is 1.42°C, slightly less than GFDLs CM2.0 model and about 0.2°C greater than the CM2.1 model (Table 1) which are among the top-performing models in the IPCC Fourth Assessment report. The MPI model of Wetzet et al. (2006) is comparable to CM2.1 with an RMS SST error of 1.27°C and the IPSL model used in Lengaigne et al. (2007) has a significantly higher error of 1.97°C. All these models have comparable errors of about 1°C in the tropics, though regional patterns are somewhat different. An area of particular interest is the Pacific cold tongue, where the *Green* model has a small positive bias, in marked contrast to the strong negative biases in the CM2 series runs. The pattern of tropical errors is quite well correlated with biases in absorbed surface radiation, reflecting the difficulty in properly simulating low stratus decks and shallow cumulus convection. RMS temperature errors in the top 1500m in the *Green* model (Figure 2c) are lower than in either of the two level coordinate models-

particularly in the Atlantic. Salinity errors (Figure 2b,d) in the *Green* model are slightly worse than in the CM2 series, possibly because this model has not been subjected to exhaustive tests of how to mix freshwater into the interior at river mouths.

Several perturbations in ocean water clarity were performed. The first (*Blue*) was the largest possible, removing all additional shortwave absorption associated with dissolved and suspended particles. The *Blue* model was run for 300 years. Additionally, four additional 120 year runs were made in which the chlorophyll concentration was everywhere reduced by 50% (*Half*), set to zero in the Pacific within 30 degrees of the equator when it was less than  $0.2 \text{ mg/m}^3$  (*BLPGyre*), set to zero in the Pacific within 5 degrees of the equator (*BLPEqu*), and set to zero within 30 degrees of the equator in all tropical regions where the average chlorophyll is greater than  $0.2 \text{ mg/m}^3$  (*BLTMarg*). The *Half* run thus can be used to evaluate the linearity of the system and the *BLPEqu* run to evaluate the impact of equatorial water clarity. The *BLPGyre* and *BLTMarg* runs examine the impact of low-productivity, oligotrophic gyre centers versus the higher-productivity, mesotrophic gyre margins overlying the oxygen minimum zones.

The perturbations we have made in these runs are quite large. This was done intentionally to set an upper limit on the additional impact of shortwave absorption due to dissolved and suspended material in different regions. As can be seen from Figure 1, the result is to produce much larger changes in heating at great depths than in previous coupled simulations- showing that the total impact of dissolved and suspended material may be significantly larger than previously realized.

In addition to the full coupled runs, a number of simulations were made with the ocean component of the model forced by the Coordinated Ocean Reference Experiment

winds and heat fluxes with a weak salinity restoring (Griffies et al., 2007). We focus here on the difference between *Green* and *Blue* ocean-only runs

### 3. Results

#### *a.) SST and wind stress changes*

That ocean water clarity has an important impact on sea surface temperature and wind stress is clearly shown in Figure 3. The net impact on SST of making ocean waters clear- illustrated by the *Blue-Green* differences in Figure 3a- is global in extent, with peak values exceeding 4°C and RMS differences of 0.6°C. The pattern shows a strong warming in the central Pacific, with cooling off-equator in the subtropical gyres (particularly in the Atlantic), strong cooling at the boundary between the subtropical and subpolar gyres, and warming in the subpolar gyres. The associated wind stress changes have a complicated pattern. Increasing equatorward winds to the north and south of the equator in the central Pacific correspond to a strengthening of the Hadley circulation. Although they cannot be seen in Figure 3a, there are also westerly wind anomalies of up to 0.02 Pa along the equator corresponding to a slackening of the easterlies exceeding 1 m/s between 140°E and 140°W and reaching a maximum of 2.2 m/s around 160°E. These changes are associated with a ~15% weakening of the Walker circulation. The northern jet stream shows a tendency to shift equatorwards. The southern jet stream shows some hint of a shift but also weakens significantly. The changes in mean winds and wind stress seen here are much larger than those seen in Shell et al. (2001), who found maximum

changes of 0.8 m/s along the equator and Lengaigne et al. (2007) who found a maximum change in wind stress of 0.004 Pa along the equator.

The magnitude of the response to changing chlorophyll is somewhat nonlinear, as might be expected from the exponential dependence of absorption. When the chlorophyll decreases by a factor of 2 (*Half* run, Figure 3b) the pattern of the SST response is reasonably similar to that produced by increasing water clarity everywhere (correlation coefficients are high globally and in the central Pacific) but the magnitude is attenuated, reaching only 35-40% of that seen in Figure 3a. The wind stresses show similar changes in the equatorial region, but less of a change in the subpolar regions.

As discussed in Anderson et al. (2007) relatively little of the response can be explained by changes in water clarity right along the equator. The pattern of SST change in *BLPEqu* simulation (in which all the additional shortwave penetration occurs in the equatorial Pacific, Figure 3c) is poorly correlated with the global *Blue-Green* difference. This is true even in the Central Pacific where the largest signals are seen. Essentially, the warming in the Eastern Pacific to the south of the equator is the only major feature reproduced. The magnitude of the SST response to changing near-equatorial shortwave penetration is quite small, of order 10% of the response to setting the water to be clear everywhere.

By contrast, in the *BLPGyre* run (in which the increased shortwave penetration occurs off-equator in the clear subtropical gyre centers, Figure 3d) a much more vigorous response with significantly higher correlation to the *Blue-Green* response is seen. This simulation reproduces the pattern of on-equatorial warming (though weakly), strong off-equatorial cooling and the shift of the gyre boundary in the North Pacific. The wind stress

response, however is much more confined to the equator than in *Blue* and does not exhibit the westerly anomalies along the equator. Essentially, the Pacific branch of the Hadley cell appears to be sensitive to the water clarity in the gyres.

The *BLTMarg* simulation (in which the additional penetration occurs in the less-clear eastern portions of the basin, Figure 3e) shows a quite different pattern, with a general warming over most of the ocean, but particularly strongly in the eastern Pacific. The winds follow this warm anomaly, which results in a strengthening of the Southern Hadley cell and a strong westerly anomaly along the equator. The Walker circulation appears to be much more sensitive to water clarity above the oxygen minimum zones than to water clarity in the subtropical gyres, while the reverse is true for the Hadley cell.

It is interesting to consider the extent to which the effects of water clarity perturbations are linear in space, by adding the SST change between *BLPGyre* and *Green* to that between *BLTMarg* and *Green*. If linearity holds, the sum will be similar to the *Blue* – *Green* difference except for changes related to high-chlorophyll regions poleward of 30S and changes in the gyres in other ocean basins. The result (Figure 3f) is a pattern that has a very high correlation with *Blue-Green* in the Central Pacific where it reproduces not only most of the spatial pattern but about 85% of the magnitude. Globally, the correlation is significantly lower, as the large warming of the subpolar gyres and cooling of the Atlantic is not reproduced- pointing to the potential importance of chlorophyll and other absorbers in these regions.

These results are very different from the ocean-only simulations presented in Anderson et al (2007), where the temperature increases are largely limited to the equatorial Pacific. One reason could be that the atmospheric feedbacks are different- a

hypothesis which we explore by looking at the relationships between surface air-sea heat fluxes and SST changes (Table 2). The regressions presented in the top row of Table 2 demonstrate that while the atmosphere in the coupled model acts to damp out SST perturbations, this damping is fairly weak on a global scale with a 1°C warming resulting in an air sea flux change of  $O(-10 \text{ W/m}^2/\text{°C})$ . The SST changes cannot be directly forced by changes in atmospheric heat flux. However, while correlation coefficients between heat flux and SST change are clearly significant (ranging from -0.48 to -0.62 on a global scale)- these number are *much* smaller than the  $O(-45 \text{ W/m}^2/\text{°C})$  decrease in air-sea heat flux (and correlations of -0.81 to -0.99) seen in the ocean-only calculations. Thus, given the same change in oceanic heat convergence, the coupled model will produce four times the SST change as the ocean-only run. Moreover in the coupled runs more than half of the spatial variance in SST change is uncorrelated with the change in heat flux- and therefore is not damped by it.

The results in the bottom half of Table 2 do show that another assumption usually made in ocean-only or hybrid coupled model runs-that of fixed shortwave radiation- is more justifiable. The shortwave feedbacks in general damp perturbations in the tropical Pacific (with a 1°C rise in SST resulting in a 5-9  $\text{W/m}^2$  decrease in absorbed shortwave radiation though with generally low correlations with the SST change). In the extratropics a 1°C rise in SST results in 2-3  $\text{W/m}^2$  *increase* in absorbed shortwave radiation- radiative feedbacks on SST changes are weakly positive. Thus while shortwave biases may cause us to overestimate the importance of chlorophyll in the cold shadow zones by allowing too much penetrating radiation to reach the ocean surface, the changes in SST do not greatly enhance the biases in cloudiness.



The water balance over the ocean also changes as the water clarity is changed (Figure 4). As with temperature, the basic pattern can be seen to consist of two main components. The first pattern, exemplified by *BLPGyre*, involves increased penetration in the clear gyre centers resulting in a strengthening of the Hadley cell (Figure 4d) producing lower salinities along the equator and higher salinities off equator in the center of the subtropical gyres. The other, exemplified by *BLTMarg* (Figure 4e), involves increased penetration above the oxygen minimum zones, producing a warming of the cold tongue and an eastward shift of the precipitation into the central Pacific, away from Indonesia. The salinity change associated with this perturbation is largely negative, with maximum freshening of  $\sim 0.6$ PSU over the central Pacific. The zero line in SSS change for *BLTMarg-Green* does not correspond to the zero line in precipitation-evaporation change- with a large region in the Southeast Pacific in which P-E change is positive showing a *decrease* in salinity. This contrasts with the somewhat better correspondence in *Blue-Green*, or *BLPGyre-Green*. This illustrates how changes in the P-E balances between gyres are much more effective at producing changes in salinity than changes in the P-E balance within gyres- where advection homogenizes water properties.

*b.) Zonal mean T,S, age*

Having sketched out the changes in surface properties, we now examine the corresponding changes in the structure of the interior ocean. The basic picture in the tropics is one in which increasing penetration of solar radiation leads to a small net cooling of the surface and a large (up to  $2.5^{\circ}\text{C}$  in the *Blue* run) warming between 100 and

400m (Figure 5a). Given that the average age of the waters at 200m depth is about 20yr, and that the additional heating rate from removing chlorophyll at 200m is around 0.07 °C/yr (Figure 1d) such a large change is roughly the right size, as waters coming from above will have experienced higher additional heating rates. These depths also become saltier (Figure 5c). One of the tracers run in these models was ideal age, a tracer which is set to 0 in the mixed layer and increases at 1 yr/yr below the mixed layer- thus giving a measure of how long it has been since water was in contact with the atmosphere.

Differences in ideal age show that increased shortwave penetration makes the water younger in the tropics (Figure 5e). The response to these changes is not linear in the chlorophyll concentration. The *Half* run shows about ¼ of the *Blue* signal in tropical temperature and salinity and exhibits an even smaller signal in age- much less than the 35-40% of the SST signal. The importance of shortwave penetration in the off-equatorial gyres is illustrated by the fact that the *BLPGyre* run has a pattern of change similar to the *Blue* run between 200 and 400m in all three fields, although the magnitude of the change is only 20-40% of that in the *Blue* run. Additionally, there is considerable penetration of warming below 400m, with the *Blue* run showing 0.6°C of warming at 600m. At these depths none of the other runs shows much of a signal.

These deep changes may be linked to changes in the Southern Ocean.

Examination of the temperature fields (Figure 5b) shows an increase in these same waters in the *Blue* run. Such changes are not seen in the other simulations, suggesting that high-latitude changes in water clarity may be important. The *Blue* run also has a significantly fresher surface Southern Ocean (Figure 5d) and an older mid-depth Southern Ocean with waters aging by up to 6 years (Figure 5f). Both *BLPGyre* and *BLTMarg* show

qualitatively similar patterns of change in salinity and age, with increasing Southern Ocean stratification in the mean. We will examine this issue in more detail in Section 3d when we consider Southern Ocean water mass formation.

*c.) Linking the changes to transport*

The differences between the *BLTMarg* and *BLPGyre* runs are quite striking- with the first run producing a net warming over most of the low latitudes and the second producing a net cooling over most of the subtropics. What accounts for the structure of the differences between these runs? Part of the answer can be seen by looking at the structure of heat export from the tropical Pacific. We examine the quantity

$$T^n = \rho c_p \sum_{k=1}^n \int v h T dx$$

where  $\rho$  is the density,  $c_p$  the specific heat,  $v$  the velocity,  $h$  the layer

thickness and  $T$  the temperature, summed over layers 1 to  $n$  and integrated zonally.  $T^n$  corresponds to the advective transport of temperature at densities lighter than layer  $n$ , converted into units of PW. This diagnostic helps isolate which water masses contribute to the total heat transport. At 23°N in the Pacific (Figure 6a,b) the *Blue* and *BLPGyre* runs show a distinct shift in the layers which transport heat polewards from those associated with the mixed layer to those associated with the upper thermocline. In *Blue* and *BLPGyre*, more heat is added to the lower part of the mixed layer, in the gyre interior, where it moves equatorwards in the interior of the gyre (compare the solid blue and green lines in Figure 6b). Most of this heat is returned in the upper thermocline in the western boundary current (compare the dashed blue and green lines in Figure 6b).

By contrast, in the *BLTMarg* run, the bulk of the heat added below the mixed layer goes into the upper thermocline in the heart of the shadow zones. Luyten, Pedlosky and Stommel, (1983) define these regions as locations where isolines of potential vorticity tend to intersect the eastern boundary rather than connecting with the mixed layer. Their theory also predicts that there should be a minimum in layer thickness (corresponding to a front in PV) along the boundary between the ventilated gyre and the shadow zone. As noted by Gnanadesikan et al. (2007) among others, this boundary is found in both the real world and models, where it corresponds to a location of sharp gradients in PV, oxygen, CFCs and ideal age- consistent with the idea that water within the shadow zones has limited advective connection to the surface. It is not surprising that heat added to this region is trapped locally. What is surprising, and should make us cautious about overinterpreting these results, is that the effect is so large when heat is added to the eastern part of the shadow zones where SST biases are large. It is possible that this sensitivity may in fact be telling us something important about why models drift, rather than about the real world.

The additional heat added below the mixed layer also makes its way to the equator, where it can also produce changes in the advective transport of heat. As shown in Figure 6c, the average temperature of water moving eastward in the Equatorial Undercurrent (defined as waters moving eastward with a velocity greater than 0.4 m/s within 3 degrees of the equator) is much higher in the *Blue* run than in the *Green*. Increasing shortwave penetration along the equator or off the equator in the clear gyres produces changes in the temperature of waters entering the EUC from the west. However, these changes are diluted by waters entering the EUC from the central Pacific. The

*BLTMarg* run, by contrast, produces an increase in the temperatures of the waters that feed the EUC in the central and Eastern Pacific. The changes in subsurface temperature are in part due to changes in the degree to which water in the upper thermocline exchanges with the mixed layer. This can be seen by looking at the changes in ideal age (Figure 6d). This tracer drops from values of 15-17 years in the *Green* run to 7-11 years in the *Blue* run. The increases in EUC temperature are clearly associated with decreases in the age of water entering the undercurrent.

*d) Tropics and subtropical wind-driven circulation*

The changes in sea surface temperatures associated with increasing water clarity result in at least three major responses in the wind stress (Figure 3). We will sketch the main features here- a more detailed analysis is currently in preparation (Anderson, Chen, Gnanadesikan and Vecchi, Atmospheric responses to changes in oceanic chlorophyll, manuscript in prep.). The first is to increase convergence along the equator, strengthening the Hadley circulation and thus intensifying the zonal winds driven by this circulation. This can be seen most clearly in the *BLPGyre* run and is associated with the already clear gyre centers. Additionally, the changes in the upper-level winds produce changes in wave activity fluxes, shifting the eddy-driven jets in mid-latitudes equatorwards so that the steep gradients in wind stress associated with the flanks of these jets intensify over the polar gyres. This effect is extremely pronounced over the subpolar North Pacific and Southern Ocean in the *Blue* run. Finally the shift in convection associated with the warming of the Eastern Equatorial Pacific (as seen in the precipitation

changes Figure 4e) results in an El Nino-like wave pattern that has its expression in the intensification of the Aleutian Low and an intensification of the low pressure over the Amundsen Sea. This last change is most strongly associated with the changes in water clarity in the *BLTMarg* simulation.

These changes in winds produce substantial changes in the wind stress curl and thus in the Sverdrup transport. Figure 7b-f shows the changes in Sverdrup transport for *Blue-Green*, *BLPEqu-Green*, *Half-Green*, *BLPGyre-Green*, and *BLTMarg-Green* simulations, with Figure 7a showing the Sverdrup transport in the *Green* control case for comparison. Note that a change of  $0.4 \text{ m}^2/\text{s}$  (the smallest colored contour interval) will correspond to a change of about 5 Sv when integrated across the Pacific Ocean. Although the changes in Sverdrup transport are smaller than the mean transport, they are nonetheless significant.

These changes have a clear effect on the upper ocean circulation. The change in the streamfunction (derived from integrating the zonal velocity along  $172^\circ\text{E}$  in the top 38 layers, Figure 8a) from *Green* to *Blue* shows a significant increase in the transport associated with the North and South Equatorial Currents, and their return flow in the EUC. Analysis of the differences in meridional transport at  $18^\circ\text{N}$ ,  $15^\circ\text{S}$  and  $25^\circ\text{S}$  (Figures 8b-d) demonstrate that they can largely be attributed to the changes in Sverdrup transport. At  $18^\circ\text{N}$  (Figure 8b), the changes are quite similar in shape for three of the models, differing primarily in magnitude, with the *Blue*, *BLPGyre* and *Half* cases producing increases in the gyre circulation of 16, 12, and 6 Sv respectively. This can be attributed to the strengthening of the Hadley cell north of the equator, resulting in an increase of the peak easterlies to the north. In the *BLTMarg* run, by contrast, there is much less

strengthening of the northern Hadley cell and a more negative wind stress curl in the eastern part of the gyre is compensated by a more positive wind stress curl in the west. The *Blue-Green* changes at this latitude are thus dominated by the changes in the relatively clear gyres.

This is not the case, however, at 10°S (Figure 8c). In the *BLPGyre* case, the enhancement of the upwelling branch of the Hadley cell results in a strengthening and slight equatorward shift in the easterly jets to the north and south of the equator (though more so in the south than in the north). This in turn results in an equatorward shift of the subtropical gyre with an increase of 12 Sv in the gyre transport at 10°S. In the *BLTMarg* case, by contrast, there is a decrease in the wind stress curl in the western Pacific, associated with the movement of the southern rain band to the east, resulting in an increase in the northward transport at this latitude. The *Blue* and *Half* cases show a mixture of these two results, predicting essentially no increase in the gyre transport. Not all of the response can be attributed to local changes in the winds- there is also an offset of about 2 Sv which is associated with a change in the Indonesian throughflow.

Moving further into the southern subtropics, we see that the dominant impact in *Blue* shifts to being associated with the tropical high-chlorophyll regions (Figure 8d). At 25°S, both the *Half* and *BLPGyre* runs show a relatively small impact on wind stress curl and transport while *BLTMarg* and *Blue* show a strong increase in northward Sverdrup transport associated with the eastward shift in precipitation (and the associated low pressure system) into the central Pacific.

*e.) Southern Ocean, SAMW/AAIW Formation*

Changes in wind stress magnitude and location over the Southern Ocean have been hypothesized to have the potential to cause significant changes in ocean ventilation and overturning (Toggweiler and Samuels, 1993,1998; Gnanadesikan and Hallberg, 2000; Toggweiler, Russell and Carson, 2006). This is especially true in low-diffusion models where wind-driven Southern Ocean upwelling represents the dominant pathway by which dense deep waters are transformed into lighter surface waters (Toggweiler and Samuels, 1998; Gnanadesikan, 1999). The large changes in wind stress magnitude in this region would thus be expected to produce significant changes in overturning circulation, as shown in Figure 9. The *Half*, *BLPGyre*, *BLTMarg*, *BLPEqu*, and *Green* runs are essentially identical, with 18 Sv of light and 22-23 Sv of dense water entering the Southern Ocean and 10-11 Sv of abyssal and 30 Sv of intermediate and mode waters leaving the region. The *Blue* run is significantly different. The supply of light water associated with the subtropical gyres increases by almost 40% to 25 Sv. The northward flow of mode and intermediate waters also increases, to about 37 Sv. As a result the mode and intermediate waters become even more dominated by the lighter watermass classes.

The fact that the overturning is so different for the *Blue* run raises the question of the role played by extratropical ocean color, which we have largely ignored until now. By trapping heat near the surface, extratropical solar absorption will tend to raise summertime temperatures while lowering wintertime temperatures. Such a temperature change could have one of two impacts. First, it could have a direct impact on watermass transformation. In order to explain the changes seen here, we would expect that the *Green*



run would have significantly less wintertime transformation of dense water than the *Blue*. Second, the changes in seasonal temperature could have an impact on the wind stress field, resulting in a change in the gyre circulation. Analysis of the transport of water lighter than 1034.5 (Figure 10a) shows that there is more creation of this water within the Southern Ocean throughout the year (suggesting that it is not the impact of temperature alone that matters). The location where the additional creation of light water occurs seems to be related to the wind stress field. The increased southward transport of light water corresponds to regions where the zonal winds are adding negative curl. The added curl is more than sufficient to explain the changes in light water transport. In February the zonally averaged wind stress increases by 0.02 Pa at 38S and decreases by an equivalent amount at 50S. The Sverdrup transport associated with such a change is  $-1.7 \text{ m}^2/\text{s}$  at 42S - 52 Sv when integrated around the globe- compared to an additional 6 Sv of light water being transported to the south. Similarly, the increased northward transport corresponds to regions where the zonal winds are adding increased positive curl.

The *BLPGyre* and *BLTMarg* perturbations, when added together, do produce a slightly enhanced southward transport of this light water, but do not show the enhancement in northward transport (Figures 10b). Neither do these low latitude perturbations reproduce the relatively large changes in the wind stress (up to 0.02 Pa in the zonal mean in some months) or in SST (changes of up to  $0.7^\circ\text{C}$ ). This suggests that it is the indirect effect of extratropical SST changes on the wind stress curl that is most important for changing the Southern Hemisphere overturning. The *Half* simulation does not show such SST changes during the wintertime, suggesting *Blue* crosses some key stability boundary allowing for more convection.

#### 4. Discussion

Although the use of perturbations in which chlorophyll is completely removed is (hopefully!) extreme- the results presented here do raise some interesting connections to other issues in earth system modeling. The first of these involves ocean physics. Because changing the profile of solar absorption can be seen as similar in effect to changes in the background mixing coefficient, moving heat vertically in the water column, our results suggest that the climate system could be very sensitive to the amount of mixing below the mixed layer. One can get a rough sense of how important this is by computing the diffusive coefficient required to match the additional shortwave flux

$$K_v^{add} = \Delta SW / (\rho c_p \partial T / \partial z) \quad (3)$$

Where  $\Delta SW$  is the change in downwelling shortwave flux,  $\rho$  is the density,  $c_p$  is the specific heat and  $\partial T / \partial z$  is the background stratification. We computed this quantity using the zonally averaged  $\partial T / \partial z$  from the *Green* simulation and computed  $\Delta SW$  using the difference between the zonally averaged flux from the *Green* simulation and the zonally-averaged flux using the same incoming radiation as in *Green* but using the penetration depth of 43m as in *Blue*. By computing the change in flux in this manner we are able to estimate the change in flux due to changing penetration alone, without considering coupled feedbacks.

As seen in Figure 11 the additional diffusion required to change the vertical heat flux as much as removing ocean color is extremely small, of order  $0.05-0.2 \times 10^{-4} \text{ m}^2/\text{s}$  for most depths below 100m, and less than  $10^{-4} \text{ m}^2/\text{s}$  below about 60m everywhere. This suggests that models could be very sensitive to small changes in either numerical of

explicit diffusivity immediately below the mixed layer base. Most coupled models, including ours, assume that once outside the zone of active mixing, the mixing coefficient immediately drops to values typical of the interior ( $0.1\text{--}0.15 \times 10^{-4} \text{ m}^2/\text{s}$ ). However, it is known that the zone immediately below the mixed layer has different internal wave properties and could therefore exhibit different mixing behavior. For example, Anis and Singhal (2006) show microstructure measurements in a freshwater lake in which the pycnocline was well defined. While they do see a marked difference between high mixing coefficients within the mixed layer and the low mixing coefficients in the pycnocline, they also find patches of high vertical diffusion below the mixed layer. Our results suggest that much more attention be paid to the impact of such near-surface turbulence patches.

Our results also suggest the possibility of some interesting coupling between the iron cycle and circulation. Iron is an important micronutrient for phytoplankton. Iron supply to the oceans is largely associated with airborne mineral dust, with the Sahara accounting for a large fraction of this supply (Li et al., 2008). These dust sources have changed markedly over time- particularly as a result of Saharan desertification. Additionally, increases in sulfur dioxide pollution (which as discussed in Fan et al., 2006 acts to increase the solubility of iron in dust) would be expected to increase chlorophyll concentrations in the North Pacific.

## **5. Summary and conclusions**

It is increasingly clear that ocean biology is far from being a passive player in the climate system. Our results show that changing water clarity can produce significant changes in the climate and circulation. This paper shows that different regions play significantly different roles in changing the pattern of surface temperature and circulation. Increasing shortwave penetration along the equator produces relatively small changes in surface temperature and circulation, with some additional warming to the south of the equator. Increasing penetration in the low-chlorophyll subtropical gyres result in strong cooling off equator and weak warming along the equator, with the potential to induce equatorward shifts of the subtropical gyres that can result in transport changes up to 20 Sv. Increasing penetration in the high-chlorophyll tropical margins has a very large impact on the temperatures throughout the shadow zones and at the surface, highlighting the potential climatic importance of these regions. The fact that these changes are larger than in previous simulations suggests that it is the modulation of heating at significant depths (100-200m) that is particularly important.

The sensitivity of the results to shortwave absorption in regions with relatively low levels of chlorophyll further highlights the importance of properly understanding the dynamics of light absorption in these regions. Parameterizations of water clarity have tended to use chlorophyll-a (Morel, 1988), in large part because in-situ measurements of this quantity are relatively easy to make. However, it has become abundantly clear in recent years that a significant fraction of shortwave absorption is due to constituents such as chromophoric dissolved organic matter (Siegel and Michaels, 1996; Siegel et al., 2005; Nelson et al. 2007; Morel et al., 2007) which can have radically different behavior than chlorophyll-a. This work suggests that a detailed examination of the differing impacts of

different absorbers on a regional basis could reveal hitherto unsuspected feedbacks between biological cycling and the climate system.

**Acknowledgements:** The authors thank the Geophysical Fluid Dynamics Laboratory for support of these runs. WGA was supported by NASA under the ECCO consortium (Grant NNG06GC28G) and the Interdisciplinary Science initiative (Grant NNX07AL801G).

We thank Steve Griffies, Laura Jackson and Andrew Wittenberg for reviewing this manuscript, Bonnie Samuels for help with the model setup and for running the control simulation, and Bob Hallberg, John Dunne, and Tony Rosati for useful discussions. Comments from Jack Barth and two anonymous reviewers are gratefully acknowledged.

## References

- Anderson, W.G., A. Gnanadesikan, R.W. Hallberg, J.P. Dunne and B.L. Samuels, 2007: Impact of ocean color on the maintenance of the Pacific Cold Tongue, *Geophys. Res. Lett.*, **34**, L11609, doi:10.1029/2007GL030100.
- Anderson, W.G., A. Gnanadesikan and A. Wittenberg, What changing ocean water clarity can tell us about tropical variability, in prep. for *Ocean Sciences*.
- Anis A., and M.A. Singhal, 2006: Mixing in the surface boundary layer of a tropical freshwater reservoir, *J. Marine Systems*, **63**, 225-243.
- Ballabrera-Poy, J., R. Murtugudde, R.-H. Zhang and A. Busalucchi, 2007: Coupled ocean-atmosphere response to seasonal modulation of ocean color: impact on interannual climate modulations in the tropical Pacific, *J. Climate*, **20**, 353-374.
- Delworth, T. and Coauthors, 2006: GFDL's CM2 global coupled climate models: Part 1- Formulation and simulation characteristics, *J. Climate*, **19**, 643-674.
- Fan, S.M., W.J. Moxim and H. Levy II, 2006: Aeolian input of bioavailable iron to the ocean, *Geophys. Res. Lett.*, **33**, L07062, doi:10.1029/2005GL024852.
- Federov, A., P. Deken, M. McCarthy, A.C. Ravelo, P.B. DeMenocal, M. Barreiro, R.C. Pacanowski and S.G.H. Philander, 2006: The Pliocene paradox- mechanisms for a permanent El Nino, *Science*, **312**, 1485-1489.
- Gent, P. and J.C. McWilliams, 1990: Isopycnal mixing in ocean models, *J. Phys. Oceanogr.*, **20**, 150-155.
- Gnanadesikan, A., 1999: A simple theory for the structure of the oceanic pycnocline, *Science*, **283**, 2077-2079.

- Gnanadesikan A. and R.W. Hallberg, 2000: On the relationship of the Circumpolar Current to Southern Hemisphere winds in large-scale ocean models, *J. Phys. Oceanogr.*, **30**, 2013-2034.
- Gnanadesikan, A., J.L. Russell and F. Zeng, 2007: How does ocean ventilation change under global warming? *Ocean Science*, **3**, 43-53.
- Griffies, S., C. Böning, and A. M. Treguier, 2007: Design considerations for coordinated ocean-ice reference experiments. *Flux News*, **3**, 3-5.
- Hallberg, R.W., 1995: A thermobaric instability of Lagrangian vertical coordinate ocean models, *Ocean Modelling*, **8**, 279-300.
- Harrison, M.J. and R.W. Hallberg, 2008: Pacific subtropical cell response to reduced equatorial dissipation, in press, *J. Phys. Oceanogr.*
- Karl, D.M., R.R. Bidigare and R.M Letelier, 2001: Long-term changes in phytoplankton community structure and productivity in the North Pacific Subtropical Gyre- The Domain Shift hypothesis, *Deep Sea Res. II*, **48**, 1449-1470.
- Lengaigne, M., C. Menkes, O. Aumont, T. Gorgues, L. Bopp, J.-M. Andre and G. Madec, 2007: Influence of the oceanic biology on the tropical Pacific climate in a coupled general circulation model, *Clim. Dyn.*, **28**, 503-516.
- Lewis, M. R., M. E. Carr, G. C. Feldman, W. Esaias, and C. McClain, 1990: Influence of penetrating solar radiation on the heat budget of the equatorial Pacific Ocean, *Nature*, **347**, 543– 545.
- Li, F., P. Ginoux, and V. Ramaswamy, 2008: Distribution, transport, and deposition of mineral dust in the Southern Ocean and Antarctica: Contribution of major sources. *J. Geophys. Res.*, **113**, D10207, doi:10.1029/2007JD009190.

- Luyten, J.L., J. Pedlosky and H.M. Stommel, The ventilated thermocline, 1983: *J. Phys. Oceanogr.*, **13**, 292-309.
- Manizza, M., C. Le Quere, A. J. Watson, and E. T. Buitenhuis , 2005: Bio-optical feedbacks among phytoplankton, upper ocean physics and sea-ice in a global model, *Geophys. Res. Lett.*, **32**, L05603, doi:10.1029/2004GL020778.
- Marzeion, B., A. Timmermann, R. Murtugudde and F.F. Jin, 2005: Biophysical feedbacks in the tropical Pacific, *J. Climate*, **18**, 58-70.
- McClain, C. R. , G. C. Feldman and S. B. Hooker, 2004: An overview of the SeaWiFS project and strategies for producing a climate research quality global ocean bio-optical time series. *Deep-Sea Res. II*, **51**, 5–42.
- Milly, P.C.D. and A.B. Shmakin, 2002: Global modeling of land, water, and energy balances, *J. Hydrometeorol.*, **3**, 283-299.
- Moore J., S. C. Doney, J. Kleypas, D. Glover, and I. Y. Fung, 2002: An intermediate complexity marine ecosystem model for the global domain. *Deep-Sea Res.*, **49B**, 403–462.
- Morel, A., 1988: Optical modeling of the upper ocean in relation to its biogenous matter content (case-I waters), *J. Geophys. Res.*, **93**, 10,749–10,768.
- Morel, A., H. Claustre, D. Antoine and B. Gentili, 2007: Natural variability of bio-optical properties in Case I waters: attenuation and reflectance in the visible and near-UV spectral domains, as observed in South Pacific and Mediterranean waters, *Biogeosciences*, **4**, 913-925.



- Murtugudde, R., J. Beauchamp, C. R. McClain, M. Lewis, and A. Busalacchi, 2002: Effects of penetrative radiation on the upper tropical ocean circulation, *J. Climate*, **15**, 470–486.
- Nakamoto, S., S. P. Kumar, J. M. Oberhuber, J. Ishizaka, K. Muneyama, and R. Frouin, 2001: Response of the equatorial Pacific to chlorophyll pigment in a mixed layer isopycnal ocean general circulation model, *Geophys. Res. Lett.*, **28**, 2021–2024.
- Nelson, N.B., D.A. Siegel, C.A. Carlson, C. Swan, W.M. Smethie and S. Khatiawala, 2007: Hydrography of chromophoric dissolved organic matter in the North Atlantic, *Deep Sea Res. I*, **54**, 710-731.
- Paytan, A. and E.M. Griffith, 2007: Marine barite-recorder of variations in ocean export productivity, *Deep Sea Res. II*, **54**, 687-705, doi:10.1016/j.dsr2.2007.01.007.
- Polovina, J. J., E. A. Howell, and M. Abecassis, 2008: Ocean's least productive waters are expanding, *Geophys. Res. Lett.*, **35**, L03618, doi:10.1029/2007GL031745.
- Reichler, T. and J. Kim, 2008: How well do coupled climate models simulate today's climate? *Bull. Amer. Met. Soc.*, **89**, 303-311.
- Schneider, E., and Z. Zhu, 1998: Sensitivity of the simulated annual cycle of sea surface temperature in the equatorial Pacific to sunlight parameterization, *J. Climate*, **11**, 1932–1950.
- Shell, K. M., S. Nakamoto, and R. C. Somerville, 2003: Atmospheric response to solar radiation absorbed by phytoplankton, *J. Geophys. Res.*, **108**(D15), 4445, doi:10.1029/2003JD003440.

- Siegel, D. A., R. R. Bidigare, and Y. Zhou, 1995: Solar radiation, phytoplankton pigments and the radiant heating of the equatorial Pacific warm pool, *J. Geophys. Res.*, **100**, 4885– 4891.
- Siegel, D.A., S. Maritorona, N.B. Nelson and M. J. Behrenfeld, 2005: Independence and interdependencies among global ocean color properties: Reassessing the bio-optical assumption, *J. Geophys. Res.*, **110**, C07011, doi:10.1029/2004JC002527.
- Siegel, D.A. and A.F. Michaels, 1996: Quantification of non-algal light attenuation in the Sargasso Sea: Implications for biogeochemistry and remote sensing, *Deep Sea Res. II*, **43**, 321-345.
- Stramska, M., and T. D. Dickey, 1993: Phytoplankton bloom and the vertical thermal structure of the upper ocean, *J. Mar. Res.*, **51**, 819– 842.
- Strutton, P.G. and F.P. Chavez, 2004: Biological heating in the equatorial Pacific,: Observed variability and potential for real-time calculation, *J. Climate*, **17**, 1097-1109.
- Sweeney, C., A. Gnanadesikan, S.M. Griffies, M.J. Harrison, A. Rosati, and B.L. Samuels, 2005: Impacts of shortwave penetration depth on large-scale ocean-circulation and heat transport, *J. Phys. Oceanogr.*, **35**(6), 1103-1119.
- Timmermann A, and F.-F Jin, 2002: Phytoplankton influences on tropical climate. *Geophys. Res. Lett.*, **29**, 2104, doi:10.10129/2002GL015434.
- Toggweiler, J.R., J. L. Russell, and S. R. Carson, 2006: Midlatitude westerlies, atmospheric CO<sub>2</sub>, and climate change during the ice ages. *Paleoceanography*, **21**, PA2005, doi:10.1029/2005PA001154.

- Toggweiler, J.R. and B.L. Samuels, 1993: Is the magnitude of the deep outflow from the Atlantic Ocean actually governed by Southern Hemisphere winds? In *The Global Carbon Cycle*, Springer-Verlag, 303-331.
- Toggweiler, J. R., and B. Samuels, 1998: On the ocean's large-scale circulation near the limit of no vertical mixing. *J. Phys. Oceanogr.*, **28**(9), 1832-1852.
- Van Oldenburgh, G.J., S.Y. Philip and M. Collins, 2005: El Nino in a changing climate: a multi-model study, *Ocean Science*, **1**, 81-95.
- Wetzel P., E. Maeier-Reimer, M. Botzet, J. Jungclaus, N. Keenlyside and M. Latif, 2006: Effects of ocean biology on the penetrative radiation in a coupled climate model, *J. Climate*, **19**, 3973-3987.
- Winton, M., R.W. Hallberg and A. Gnanadesikan, 1998: Simulation of density-driven downslope flow in z-coordinate ocean models, *J. Phys. Oceanogr.*, **28**, 2163-2174.

## Figure Captions

**Figure 1:** Structure of chlorophyll-dependent shortwave heating. (a) Penetration depths for Manizza et al. (2005) scheme using a SeaWiFS-based chlorophyll-a climatology. Contours between 5m and 23 correspond to values associated with previous work. Wetzel et al. (2006) used a baseline of 11m, Murtugudde et al. (2001) a baseline of 17m, Jerlov (1969) type I water has an e-folding scale of 23m. (b) Penetration depth for the scheme of Moore et al. (2002). (c) Heating rates ( $^{\circ}\text{C}/\text{yr}$ ) for an incoming solar radiation of  $200 \text{ W}/\text{m}^2$  at 100m depth along a section at  $140^{\circ}\text{W}$ . (d) Same as (c) but at 200m.

**Figure 2:** Errors (compared with the World Ocean Atlas regridded to the model grid) in the control simulation averaged over years 200-300. (a) Sea surface temperature in  $^{\circ}\text{C}$ . (b) Sea surface salinity in PSU. (c) RMS error in temperature ( $^{\circ}\text{C}$ ) 0-1500m. (d) RMS error in salinity (PSU) 0-1500m.

**Figure 3:** Sea surface temperature ( $^{\circ}\text{C}$ ) and wind stress changes from changing ocean water clarity for years 41-120. Numbers show the correlation and regression coefficients for the SST difference vs. the *Blue-Green* difference- enabling evaluation of which regions are most important for producing the changes in the *Blue* run. First number is for globe, second for tropics. (a) *Blue-Green*. (b) *Half-Green* (c) *BLPEqu-Green* (d) *Limit\_02-Green* (e) *BLTMarg-Green* (f)  $(\text{BLTMarg-Green}) + (\text{BLPGyre} - \text{Green})$ .

**Figure 4:** Precipitation-Evaporation (in m/yr, colors) and sea surface salinity (contours, interval 0.2 PSU, thick solid line corresponds to zero contour, solid lines are positive, dashed lines are negative) changes relative to *Green* run for years 41-120 of the simulations. Correlation and regression coefficients of the change compared with *Blue-Green* are shown by the numbers below each plot. (a) *Blue-Green*. (b) *Half-Green* (c) *BLPEqu-Green* (d) *BLPGyre-Green* (e) *BLTMarg-Green* (f) *(BLTMarg-Green)+(BLPGyre -Green)*.

**Figure 5:** Upper ocean changes in temperature (°C), salinity (PSU) and ideal age (years) relative to *Green* simulation resulting from changes in ocean water clarity for years 81-120 of the simulations. (a) Temperature, 30S-30N. (b) Temperature, 90S-30S. (c) Salinity, 30S-30N. (d) Salinity, 90S-30S. (e) Ideal age, 30S-30N. (f) Ideal age, 90S-30S.

**Figure 6:** Changes in heat transport and circulation associated with changing the shortwave penetration depth, years 41-120. (a) Cumulative normalized temperature transport in the vertical ( $Q_T^k = \sum_{n=0}^k \int_x \rho c_p v_n T_n h_n dx$ ) at 23N in the model suite. Note the large differences between the *Blue* and *BLPGyre* simulations and the other simulations. b.) Cumulative normalized temperature transport in the meridional direction

$$Q_T(x) = \int_{x'=100E}^x \sum_{n=ki}^{kf} \rho c_p v_n T_n h_n dx'. \text{ Solid lines show cumulative transport in the lower mixed layer (layers 2-4) dashed lines cumulative transport in the upper pycnocline. c.) Average temperature of water in the Equatorial Undercurrent (EUC) defined as water moving}$$

layer (layers 2-4) dashed lines cumulative transport in the upper pycnocline. c.) Average temperature of water in the Equatorial Undercurrent (EUC) defined as water moving

eastward at a speed exceeding 0.4m/s within 3 degrees of the equator. d.) Average ideal age of water in the EUC.

**Figure 7:** Sverdrup transport in  $\text{m}^2/\text{s}$  and its changes in  $\text{m}^2/\text{s}$  in the model suite for years 41-120 of the simulations. (a) Control transport from *Green* run ( $4 \text{ m}^2/\text{s}$  contour). Changes in transport ( $0.4 \text{ m}^2/\text{s}$  contour) are shown for (b) *Blue-Green* (c) *Half-Green* (d) *BLPEqu-Green* (e) *BLPGyre-Green* and (f) *BLTMarg-Green*.

**Figure 8:** Change in horizontal circulation associated with water clarity changes, dashed lines show integrated Sverdrup flux. All transports are in the top 38 layers (eliminating effects of bottom torques). (a) Eastward transport integrated along  $172^\circ\text{E}$  for four different models. (b) Northward transport integrated across the Pacific at  $18^\circ\text{N}$ . (c) Northward transport integrated across the Pacific at  $10^\circ\text{S}$ . (d) Northward transport integrated across the Pacific at  $25^\circ\text{S}$ .

**Figure 9:** Overturning at  $30^\circ\text{S}$ , years 41-120. Left: Fluxes in each density class in Sv. Right: Overturning streamfunction in Sv integrated from lightest layers downwards. Note the difference in transport between *Blue* and the other simulations.

**Figure 10:** Changes in the northward transport of light water related to surface quantities over the course of the year. (a) Zonally integrated light water transport change in Sv (colors) and zonally averaged surface wind stress change in Pa (contours) between the *Blue* and *Green* runs. Note how light water transport change follows wind stress changes.

(b) Same as (a) but for  $(BLPGyre-Green) + (BLTMarg - Green)$ . Note that the additional northward transport is not seen, nor are the changes in zonally integrated wind stress. (c) Same as (a) but with contours of zonally averaged SST change overlaid. (d) Same as (b) but with contours of zonally averaged SST change overlaid.

**Figure 11:** Diffusion coefficient (in  $10^{-4} \text{ m}^2/\text{s}$ ) that would produce a vertical heat flux equivalent to the additional shortwave flux caused by changing  $k_{bg}$  from the value used in *Green* to the value used in *Blue*.

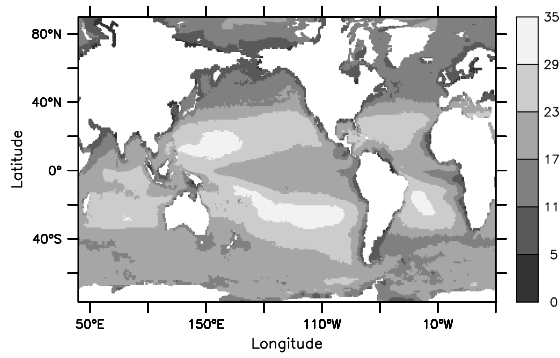
Property	<i>Green</i> (Isopycnal)	CM2.0 (Level)	CM2.1 (Level)
RMS SST Error Global	1.42	1.49	1.23
90S-30S	1.58	1.31	1.42
30S-30N	1.26	1.05	1.04
30N-90N	1.62	2.60	1.41
RMS Temperature Error 0-1500m	1.31	1.71	1.42
Mean SSS Bias	-0.48	-0.43	-0.20
RMS SSS Error	0.99	1.04	0.87
RMS Salinity Error 0-1500m	0.38	0.37	0.33
SST Bias 180W-100W, 2S-2N	0.28	-0.90	-0.70

**Table 1:** Control model compared with GFDL's two global coupled climate models run for the Fourth Assessment report. Temperature Errors and biases are in °C, salinity errors and biases in PSU.

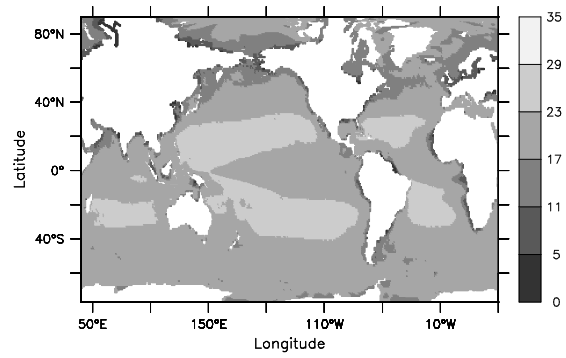


	Blue-Green	BLPGyre-Green	BLTMarg-Green	BLPEqu-Green	Blue-Green Ocean-only
$\Delta\text{SST}-\Delta\text{HF}$ , Global	-12.5 (-0.62)	-10.8 (-0.55)	-12.0 (-0.52)	-12.4 (-0.48)	-43.1 (-0.89)
$\Delta\text{SST}-\Delta\text{HF}$ , 90S-30S	-11.4 (-0.56)	-13.4 (-0.63)	-7.3 (-0.38)	-11.2 (-0.45)	-44.1 (-0.86)
$\Delta\text{SST}-\Delta\text{HF}$ , 30S-30N , 80W-120E	-13.5 (-0.55)	-7.1 (-0.44)	-25.5 (-0.86)	-12.3 (-0.43)	-47.0 (-0.98)
$\Delta\text{SST}-\Delta\text{HF}$ , 30S-30N 120E-80W	-13.6 (-0.65)	-10.9 (-0.52)	-9.3 (-0.42)	-12.4 (-0.45)	-48.5 (-0.99)
$\Delta\text{SST}-\Delta\text{HF}$ , 30N-90N	-11.9 (-0.70)	-18.0 (-0.82)	-10.0 (-0.50)	-16.9 (-0.71)	-28.5 (-0.81)
$\Delta\text{SST}-\Delta\text{SW}$ , Global	-1.2 (-0.10)	-2.0 (-0.15)	-2.6 (-0.21)	-2.3 (-0.16)	
$\Delta\text{SST}-\Delta\text{SW}$ , 90S-30S	2.6 (0.36)	1.1 (0.17)	1.5 (0.18)	1.5 (0.16)	
$\Delta\text{SST}-\Delta\text{SW}$ , 30S-30N, 80W-120E	2.5 (0.18)	0.5 (0.04)	-4.6 (-0.43)	-7.9 (-0.46)	
$\Delta\text{SST}-\Delta\text{SW}$ , 30S-30N 120E-80W	-8.9 (-0.54)	-5.2 (-0.28)	-5.5 (-0.34)	-5.0 (-0.26)	
$\Delta\text{SST}-\Delta\text{SW}$ , 30N-90N	2.7 (0.41)	1.8 (0.30)	2.7 (0.37)	2.4 (0.38)	

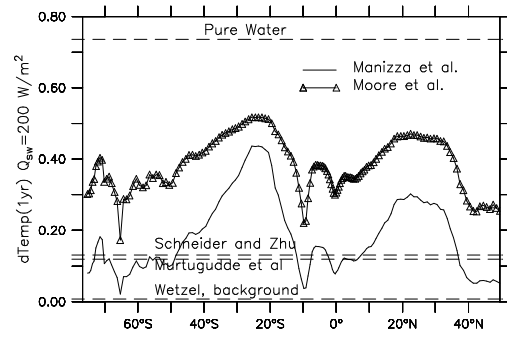
**Table 2:** Regression coefficients in  $\text{W/m}^2/^\circ\text{C}$  and correlations (in parentheses) between differences in SST ( $\Delta\text{SST}$ ) and differences in total air-sea heat fluxes ( $\Delta\text{HF}$ ) and net shortwave flux ( $\Delta\text{SW}$ ) associated with changes in ocean water clarity. Regressions are broken down by the region over which the perturbation is applied (columns) and the region over which the response is evaluated (rows). Negative values show that atmospheric thermodynamic feedbacks act to damp the SST perturbation (reducing the flux into the ocean if the ocean warms), positive values show that they would reinforce it.



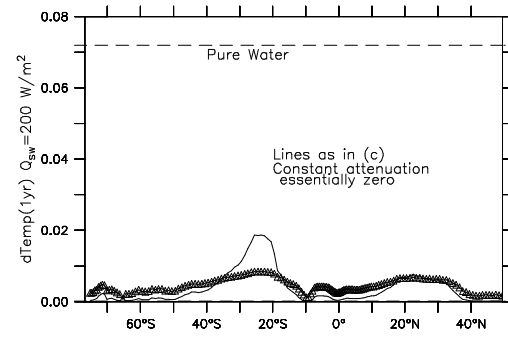
(a)  $Z_{\text{pen}}$  (m): Manizza et al. (2005)



(b)  $Z_{\text{pen}}$  (m): Moore et al. (2002)



(c) Heating rate at 140W, 100m



(d) Heating rate at 140W, 200m

**Figure 1**

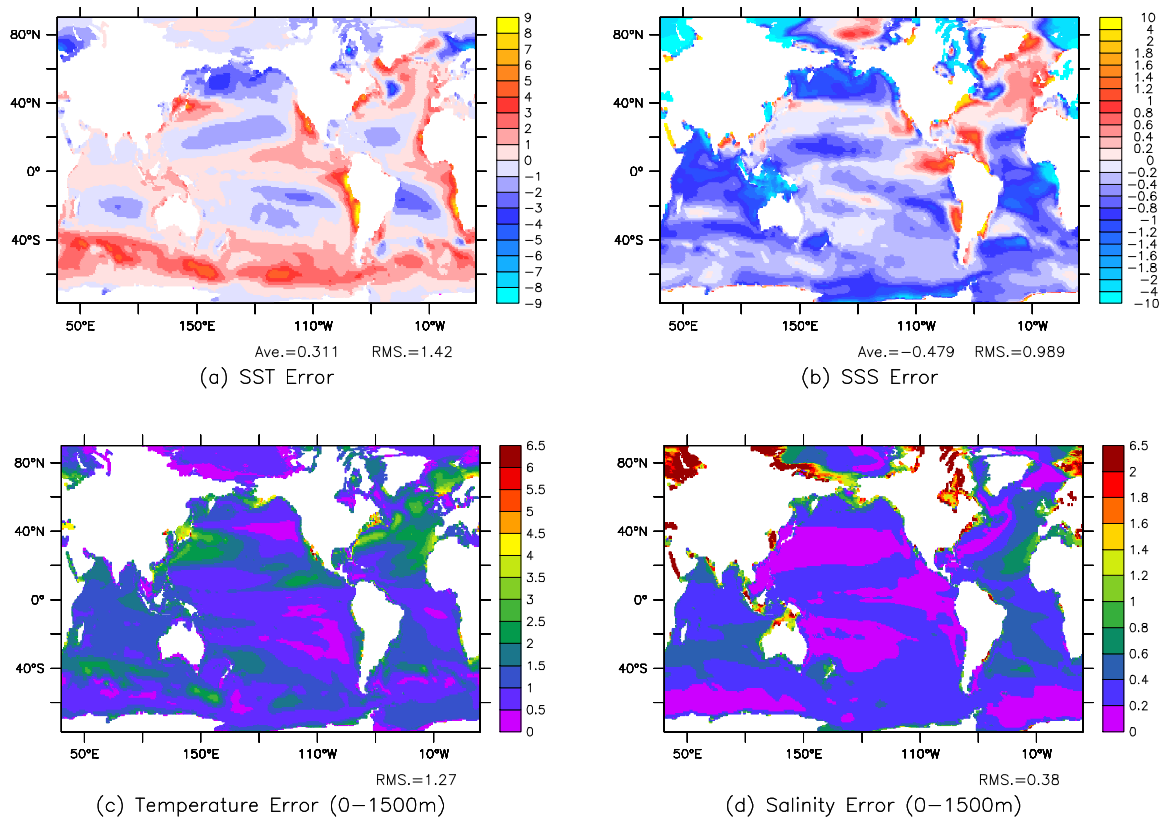


**Figure 2**

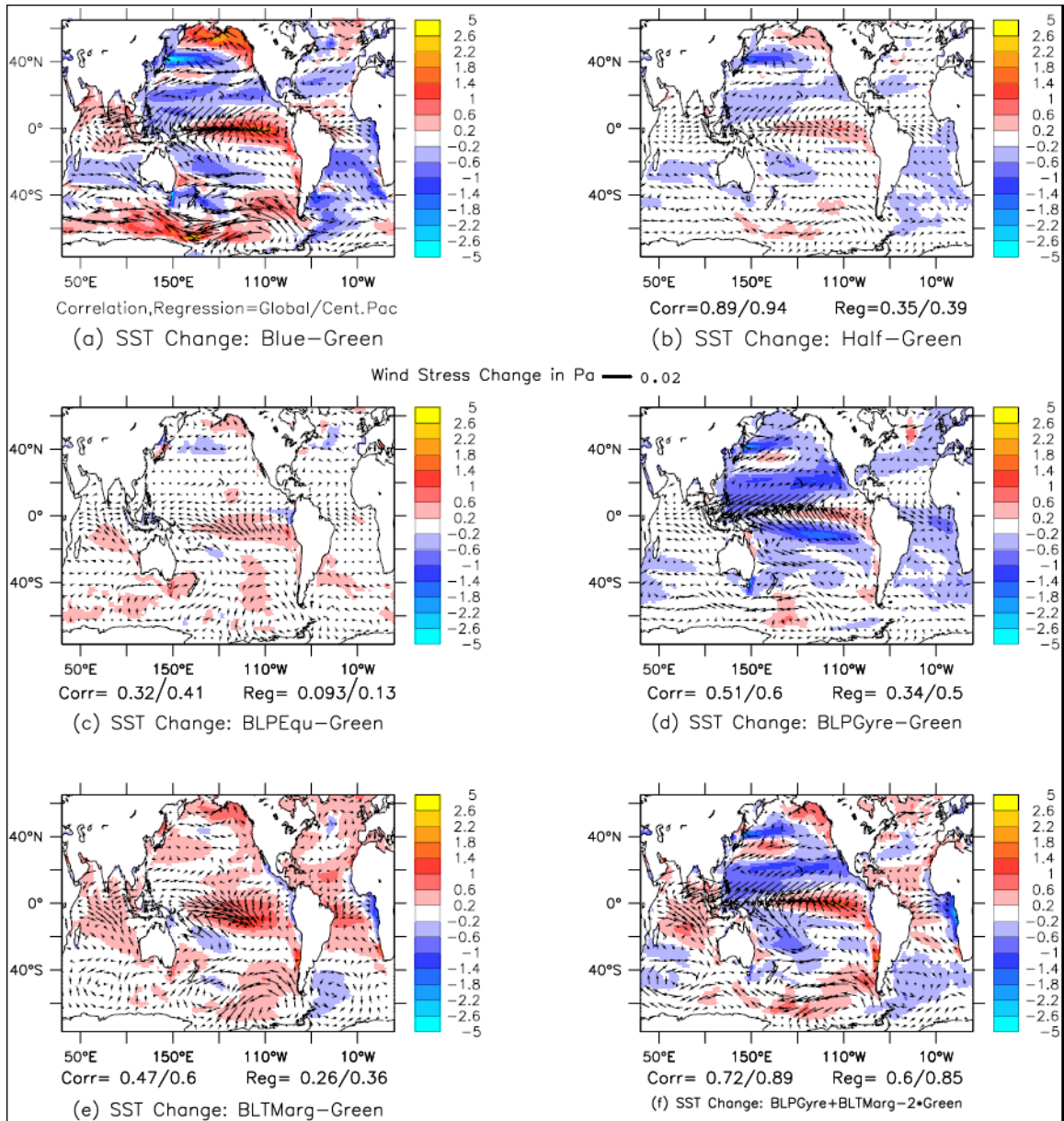


**Figure 3**

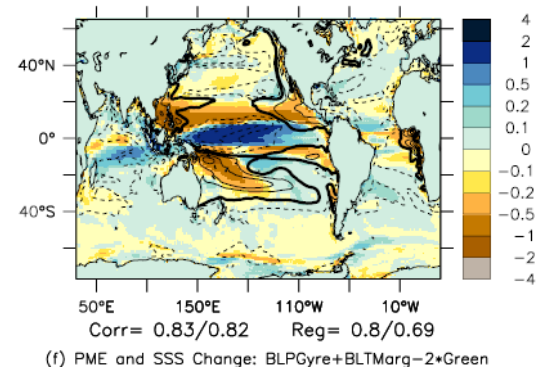
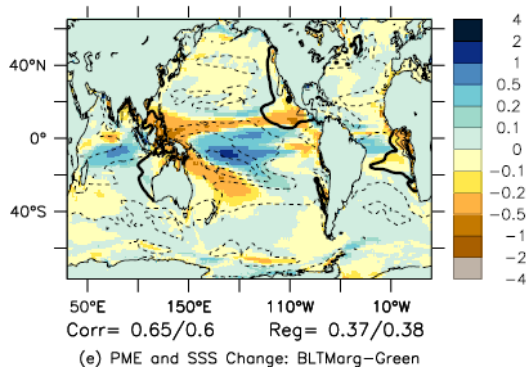
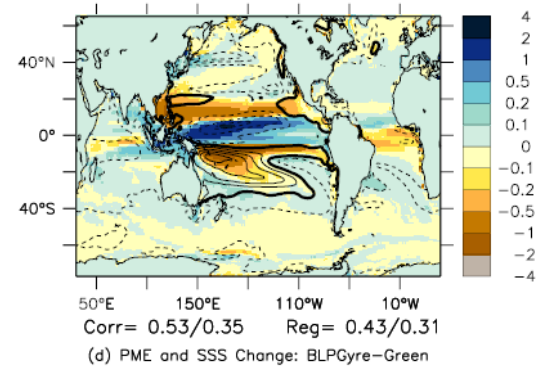
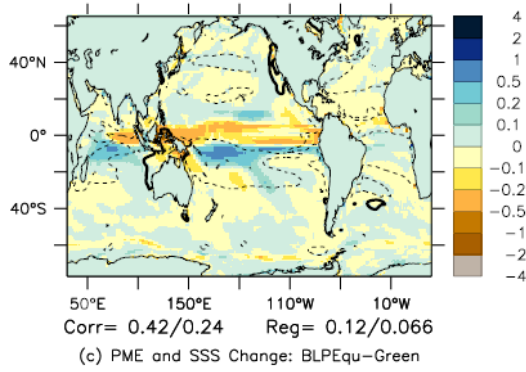
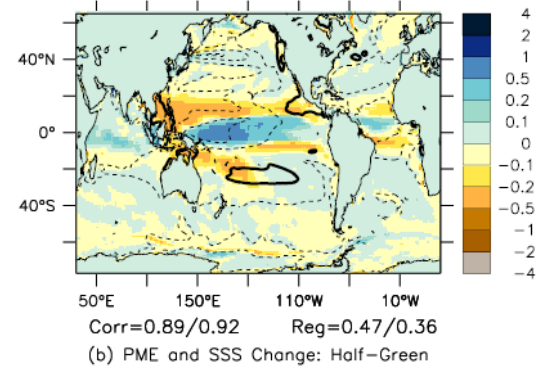
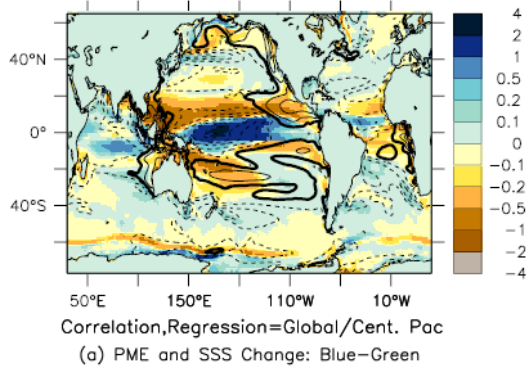
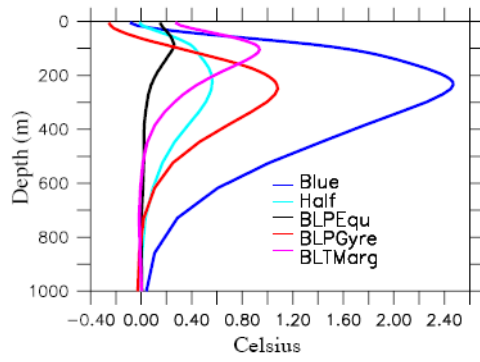
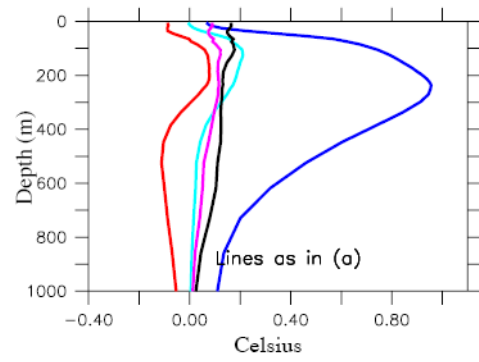


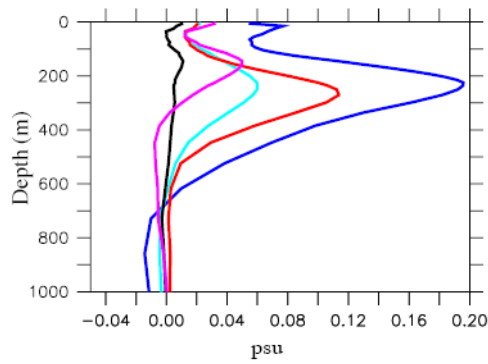
**Figure 4**



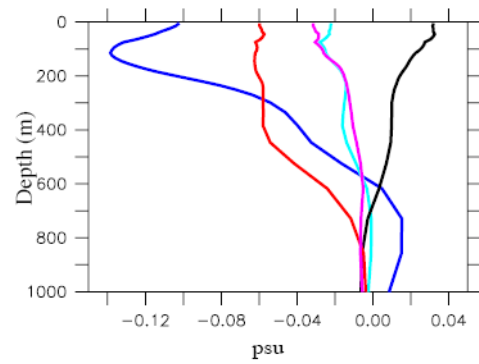
(a) Temp vs. Green 30S-30N



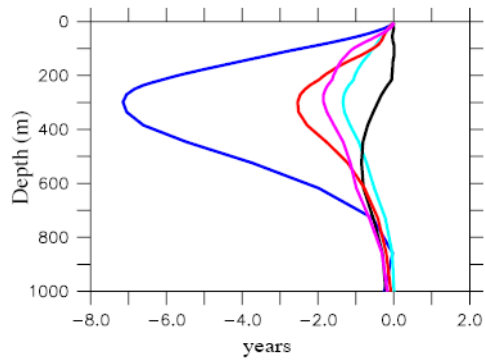
(b) Temp vs. Green 90S-30S



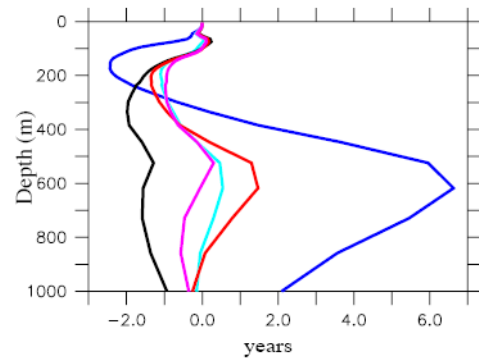
(c) Salt vs Green, 30S-30N



(d) Salt vs Green 90S-30S



(e) Age vs Green 30S-30N



(f) Age vs Green 90S-30S

**Figure 5**

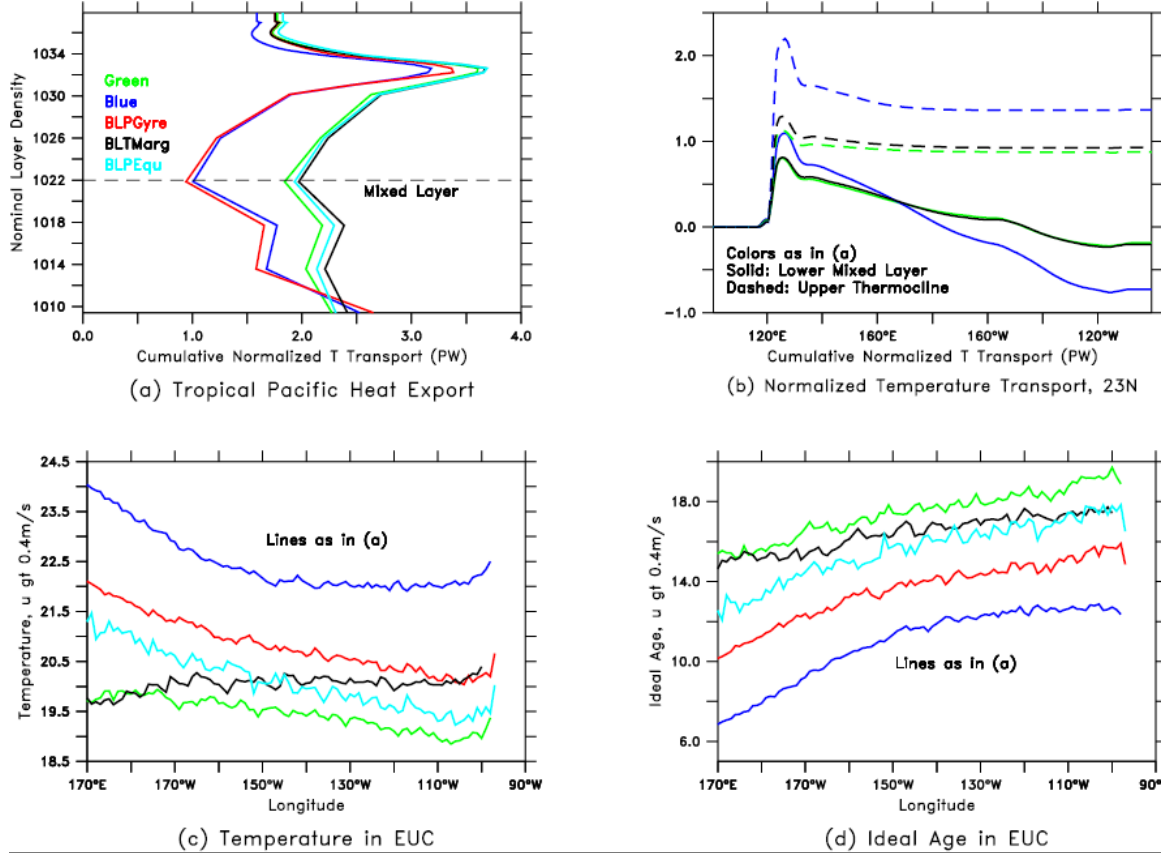


**Figure 6:** Changes in heat transport and circulation associated with changing the shortwave penetration depth, years 41-120. (a) Cumulative normalized temperature transport in the vertical ( $Q_T^k = \sum_{n=0}^k \int \rho c_p v_n T_n h_n dx$ ) at 23N in the model suite. Note the large differences between the *Blue* and *BLPGyre* simulations and the other simulations.

b.) Cumulative normalized temperature transport in the zonal direction

$$Q_T(x) = \int_{x'=100^\circ E}^x \sum_{n=ki}^{kf} \rho c_p v_n T_n h_n dx'.$$

Solid lines show cumulative transport in the lower mixed layer (layers 2-4) dashed lines cumulative transport in the upper pycnocline. c.) Average temperature of water in the EUC (moving eastward at a speed exceeding 0.4m/s) within 3 degrees of the equator. d.) Average ideal age of water in the EUC.

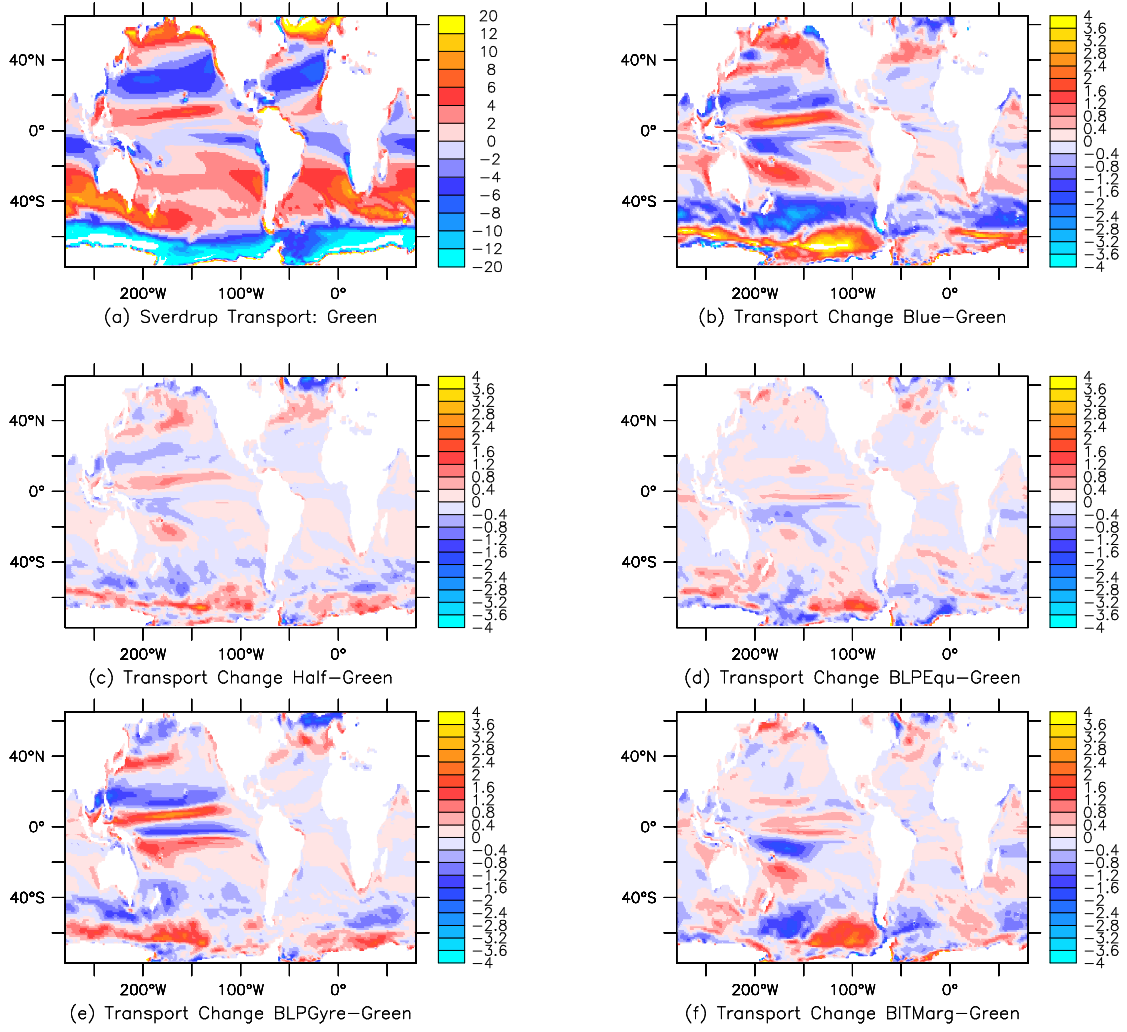


**Figure 7**



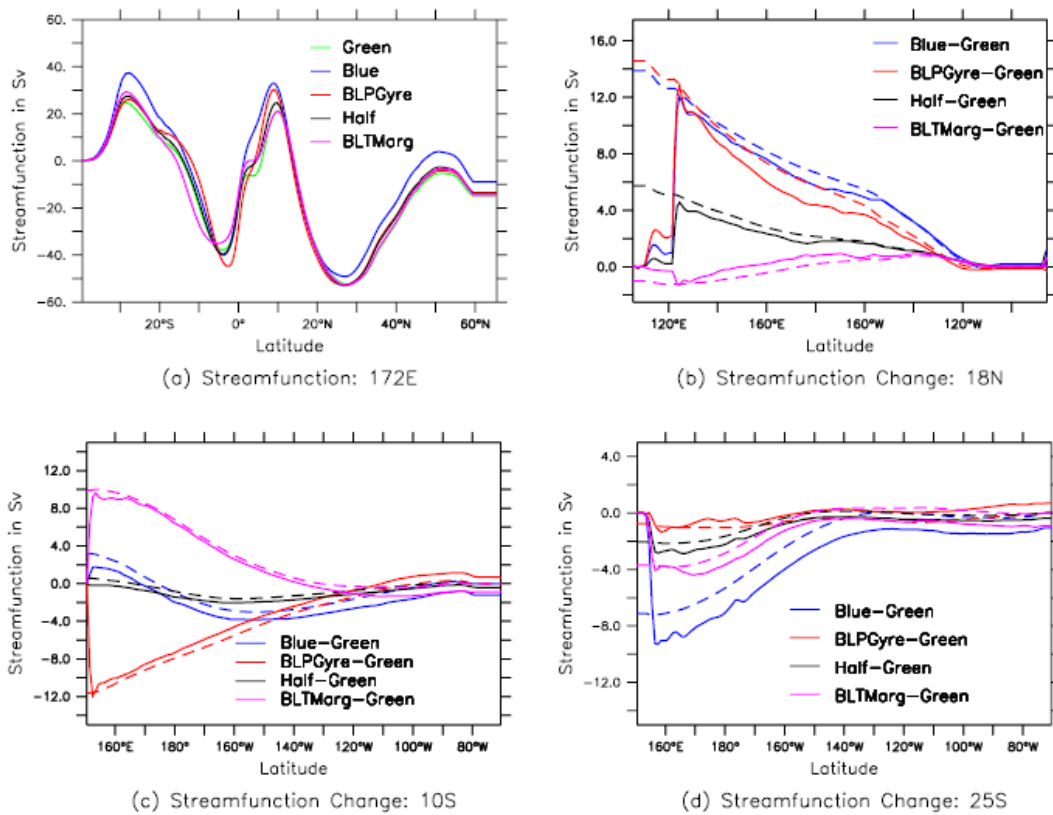


**Figure 8.**

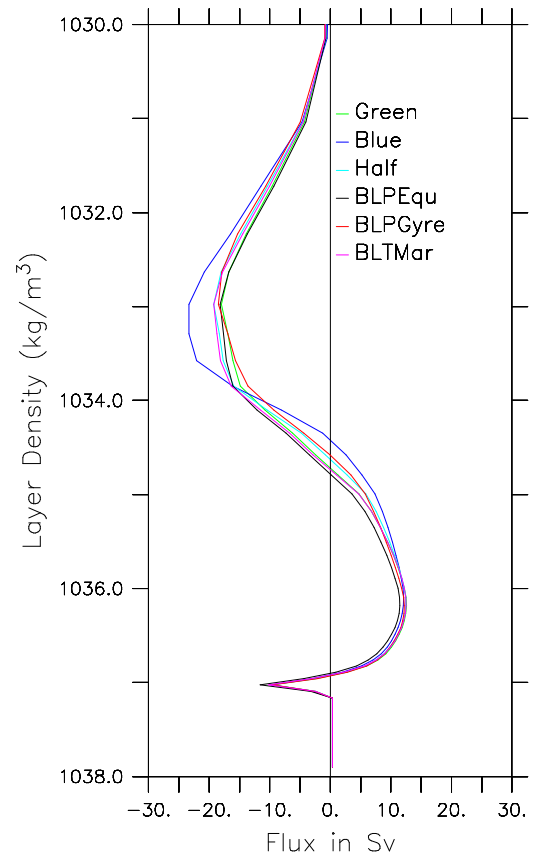
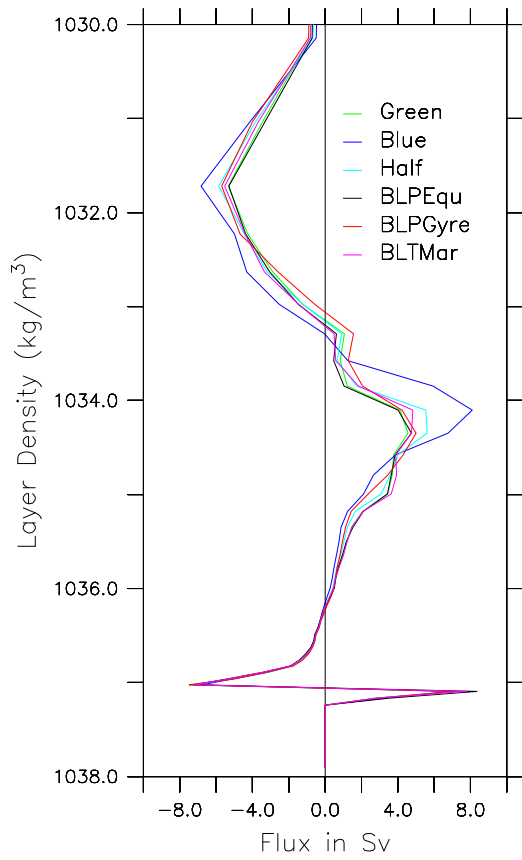


**Figure 9**



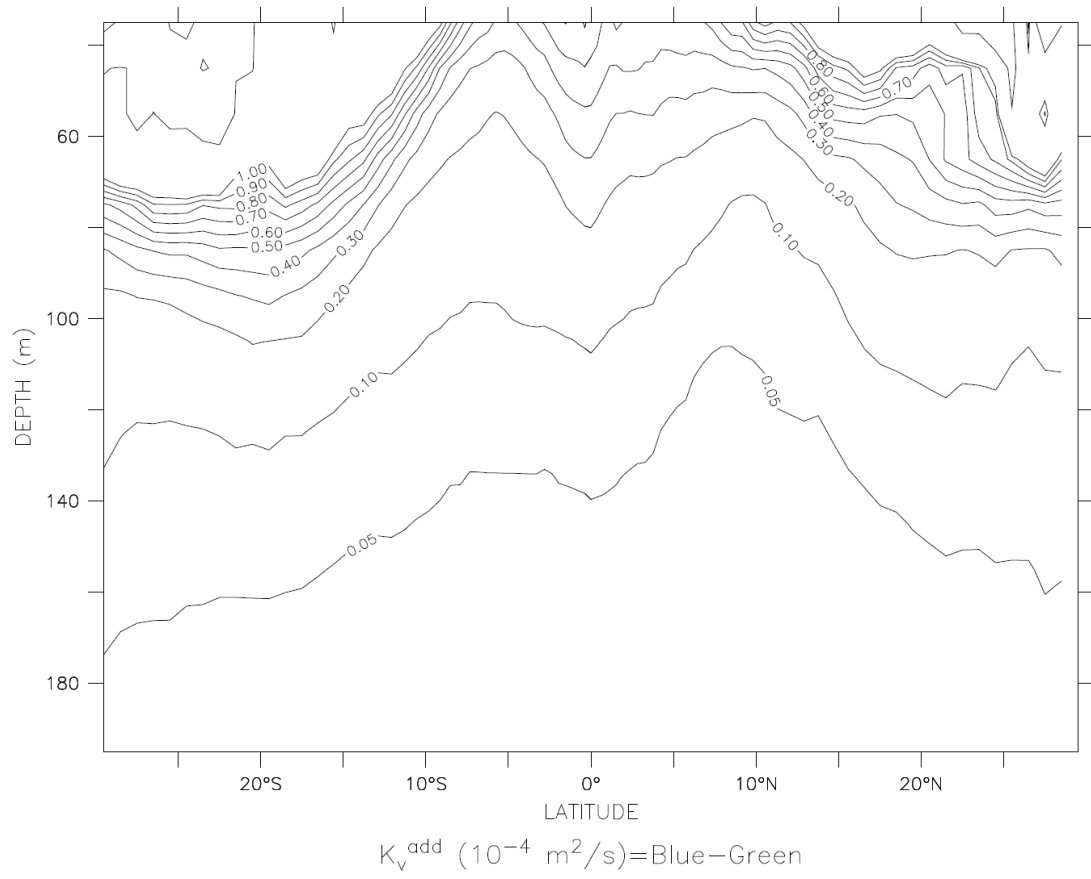


**Figure 11**